Nano Express

INCLUSIVE PUBLISHING
TRUSTED SCIENCE

PAPER • OPEN ACCESS

Investigating the mechanical behavior of hydroxyapatite-reduced graphene oxide nanocomposite under different loading rates

To cite this article: Hassan Nosrati *et al* 2020 *Nano Ex.* **1** 010053

View the article online for updates and enhancements.

You may also like

- Single cell mechanics analyzed by atomic force microscopy and finite element simulation
Xiaobo Peng, Leqian Zhao, Qiping Huang et al.
- Unfolding force definition and the unified model for the mean unfolding force dependence on the loading rate
Rafayel Petrosyan
- Surface damage mechanics of WC/Co composites investigated by indentation and diamond scratch
Quanli Zhang, Zhen Zhang and Yucan Fu

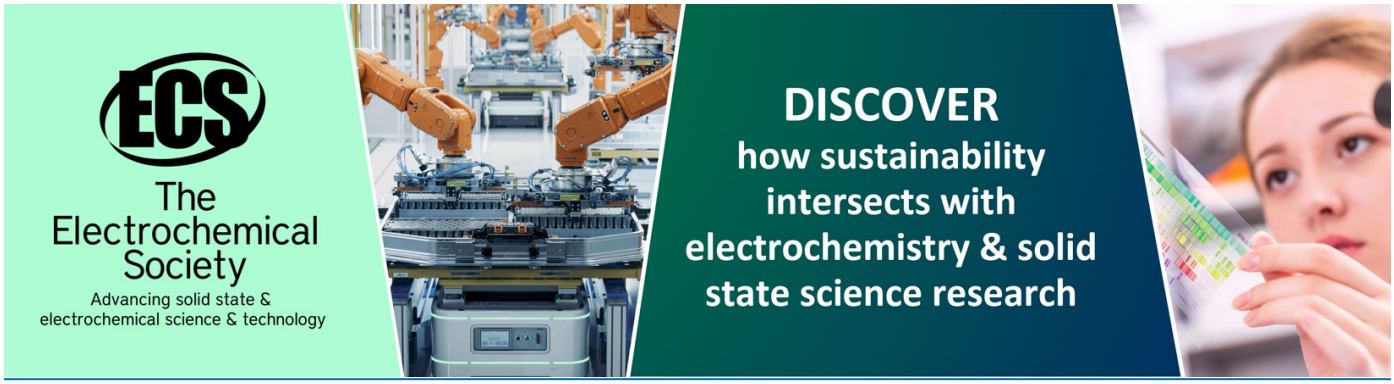

This content was downloaded from IP address 3.128.171.246 on 12/05/2024 at 07:15

NANO EXPRESS

PAPER

Investigating the mechanical behavior of hydroxyapatite-reduced graphene oxide nanocomposite under different loading rates

Hassan Nosrati[1], **Rasoul Sarraf-Mamoory**[1], **Dang Quang Svend Le**[2], **Amir Hossein Ahmadi**[3], **Maria Canillas Perez**[4] **and Cody Eric Bünger**[2]

[1] Department of Materials Engineering, Tarbiat Modares University, Tehran, Iran
[2] Department of Clinical Medicine, Aarhus University, Denmark
[3] Department of Basic Science, Shahed University, Tehran, Iran
[4] Instituto de Cerámica y Vidrio, CSIC, Madrid, Spain

E-mail: rsarrafm@modares.ac.ir

Keywords: Vickers indentation, hydroxyapatite, nanocomposite, reduced graphene oxide

OPEN ACCESS

RECEIVED
6 April 2020

REVISED
26 May 2020

ACCEPTED FOR PUBLICATION
2 June 2020

PUBLISHED
17 June 2020

Original content from this work may be used under the terms of the Creative Commons Attribution 4.0 licence.

Any further distribution of this work must maintain attribution to the author(s) and the title of the work, journal citation and DOI.

Abstract

In this study, the hydroxyapatite (HA)-reduced graphene oxide (rGO) nanocomposite was investigated for its mechanical properties. The nanocomposite used in this study was made in two stages. The HA-rGO powders were first synthesized by hydrogen gas injected hydrothermal method, and then consolidated by spark plasma sintering. HA-rGO nanocomposite was subjected to Vickers indentation experiments with different loading rates. Various analyzes have been used in this study, including x-rays diffraction, field emission scanning electron microscopy, high-resolution transmission electron microscopy, fast fourier transform, and inverse fast fourier transform. The findings of this study showed that the HA in this nanocomposite was reinforced with rGO sheets coated with HA. As the loading rate increased, the slope of the curves in the elastic region was increased, indicating that the elastic modulus was increased. Also, the contact depth at higher loading rates was increased. Plastic deformation was higher at higher loading rates and the hardness had increased. As the loading rate increased from 300 mN to 1 N, the hardness and elastic modulus increased with more slope than when the loading rate changed from 1 N to 2 N. The presence of rGO sheets had partially controlled the HA brittleness.

1. Introduction

Applications of biomaterials are expanding rapidly because they are associated with human health. As a result, the advancement and improvement of medical materials and devices will always be growing. Medical materials are usually implanted in the body through surgery, which requires high precision in their design. Therefore, examination of the properties of biomaterials is among the most important medical challenges. In particular, materials used as implants must have biocompatibility properties [1, 2]. Among the biomaterials known so far, HA and its composites have received much attention and among the HA composites, nanocomposites using carbon materials have shown more interesting properties. Research on carbon nanomaterials-HA nanocomposites is extremely expanding. Carbon nanomaterials include graphene sheets, graphene oxide (GO), carbon nanotubes, graphene nanoribbones, and nanodiamonds along with HA are the main phases of these nanocomposites [3–7]. Among the carbon nanomaterials, graphene has received more attention than others because of its unique properties such as good biocompatibility and excellent mechanical properties. Graphene plays a reinforcing role in graphene-HA nanocomposites. High specific surface area with honeycomb structure and thickness of about one carbon atom has made graphene excellent reinforcing properties [8–11]. Graphene has been used as a reinforcing phase to overcome the weakness of the mechanical properties of HA. HA is inherently brittle, has low fracture toughness and low wear resistance despite its excellent biocompatibility, bioactivity, non-toxicity and similarity to bone mineral composition. Therefore, reinforcing phases are added to eliminate mechanical weaknesses [12–15].

© 2020 The Author(s). Published by IOP Publishing Ltd

One of the synthesis methods for graphene-HA nanocomposites is the use of hydrothermal process. In this method, the rGO-HA nanostructured powders are first synthesized by hydrothermal method at high temperature and pressure [16–19]. These powders subsequently consolidated by various methods such as spark plasma sintering (SPS). The rGO sheets obtained in this method are the GO sheets that are reduced in the hydrothermal process and converted to rGO. Previous researches have shown that the addition of graphene sheets to HA improves the mechanical and biological properties of HA. Adding a small amount of graphene sheets (up to 1%) has significantly increased the mechanical characteristics of HA (compression strength and fracture toughness). The addition of graphene sheets has also improved the biological properties under *in vitro* conditions, although more research is needed under *in vivo* conditions. In all published reports, the mechanical behavior of these nanocomposites against the specified amount of loading has been investigated, but no report has been published on the mechanical behavior of these materials against load changes [20–23]. The mechanisms that lead to increased fracture toughness in these nanocomposites include graphene pull-out, crack deflection, graphene bridging, and inhibition of crack growth by graphene sheets [24, 25]. One of the mechanical properties indicators of materials is their behavior against the variable loads applied to the materials at varying rates. Indentation (micro and nano) is one of the methods to obtain the mechanical properties (hardness, elastic modulus, and fracture toughness) of ceramics, which is performed by various indenters such as Vickers and Berkovich indenters [26–33].

In a previous published study, rGO (1.5%wt)-HA nanocomposite was prepared by high pressure hydrothermal process followed by the spark plasma sintering method. The results showed that the interfaces between the rGO sheets and the HA were coherent. Also, indentation analysis with nanoindentation method showed that the mechanical properties of this nanocomposite were significantly increased compared to pure HA [34]. The main purpose of this study is to investigate the mechanical behavior of HA-rGO nanocomposites against the load changes. For this purpose, HA-rGO powders were first synthesized by a hydrothermal method and then consolidated by SPS. The fabricated nanocomposite was subjected to a Vickers indentation experiments with different loading rates. Various analyzes have been used in this study, including x-ray diffraction (XRD), X-ray photoelectron spectroscopy (XPS), field emission scanning electron microscopy (FESEM), high-resolution transmission electron microscopy (HRTEM), fast fourier transform (FFT) and inverse fast fourier transform (IFFT). The findings of this study could be useful for applications of this nanocomposite.

2. Experimental

2.1. Preparation of GO

GO was synthesized by the Hummers' method. Briefly, 2 g of graphite powders was added to 46 mL of H_2SO_4 (98%) and was stirred for 1 h. Then, 6 g of $KMnO_4$ was added gradually and was stirred for 2 h at 35 °C. Then, 92 mL of water was added slowly. The mixture was stirred for 1 h and diluted with 280 mL of water. Then, 10 mL of H_2O_2 (35%) was added dropwise. The resulting GO suspension was left overnight. The remaining GO suspension was washed by centrifugation, with HCl and acetone, and water. Finally, the precipitation of GO was dried in a vacuum oven at 60 °C for 24 h [23, 35].

2.2. Preparation of HA-rGO nanocomposite

The solution containing calcium ions (4.7 grams of calcium nitrate tetrahydrate in 120 mL of water) was added dropwise to a 20 mL stirred suspension of GO (HA/1.5% rGO) with stirring continued for 1 h. The solution containing phosphate ions (1.56 grams of diammonium hydrogenphosphate in 80 mL of water) was dropwise added to the solution and the pH was adjusted to 11 with ammonium solution. Then, the resulting solution was poured into the Teflon vessel and transferred to the hydrothermal autoclave (5 h at 180 °C by injection of hydrogen gas at 10 bar). The resulting powders were dried at oven for 24 h at 60 °C. Then, the synthesized powders were consolidated by SPS method (950 °C, 50 MPa). The specifications of the chemicals and hydrothermal system used in this study have been published in previous reports [34]. Instrumented microindentation experiments were conducted on the polished surfaces of samples using Grindosonic tester with a Vickers tip at a maximum load of 300 mN, 1 N, and 2 N (ramp dwell time of 10 s). Figure 1 shows the time-temperature-displacement-sintering speed diagram for SPS process, indentation affected zone, load-displacement diagram, and load-time diagram. According to these diagrams (figure 1(a)), the displacement value is ultimately about 2 mm. The distortions observed in the 900 °C temperature range correspond to the critical temperature of the sintering. After sintering, nine tests were performed at different locations of each sample by the Vickers indentation technique (figure 2(b)). Elastic modulus and hardness were calculated from the load-displacement curves (figure 2(c)) using Oliver-Pharr method [36].

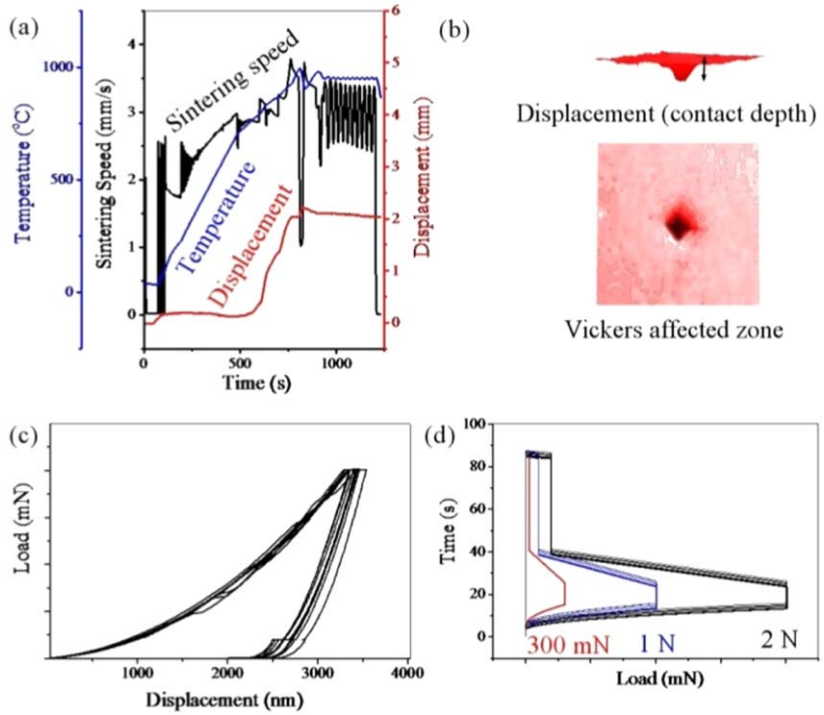

Figure 1. (a) Time-temperature-displacement-sintering speed diagram for SPS process, (b) indentation affected zone, (c) load-displacement diagram, (d) load-time diagram.

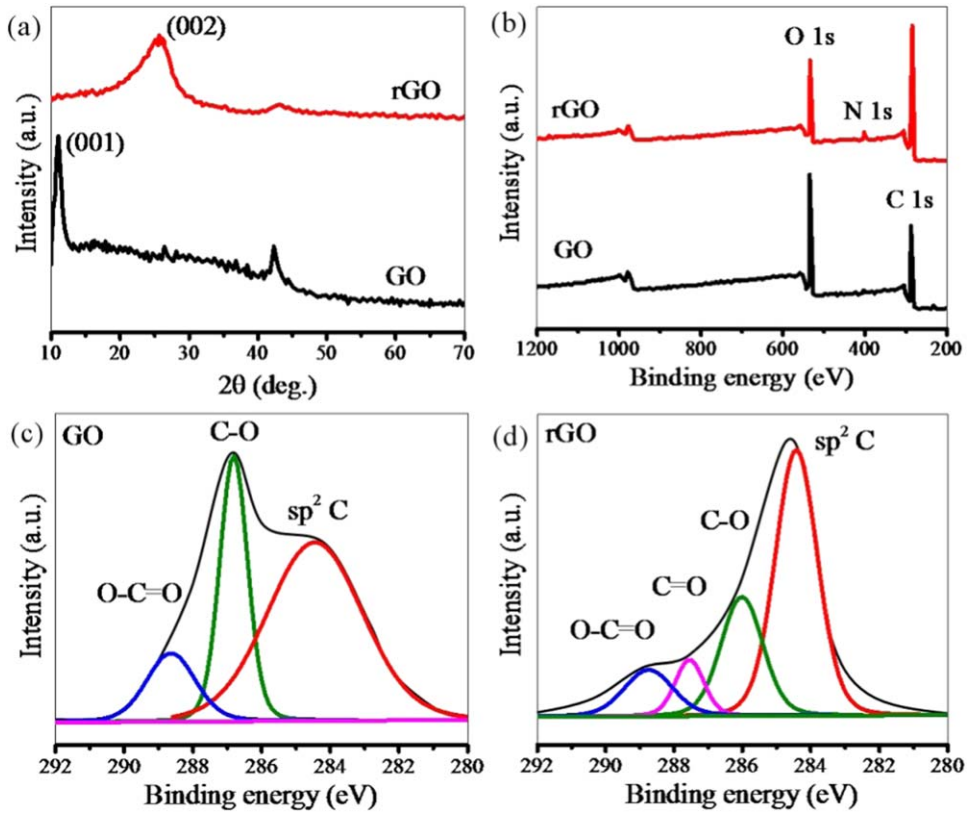

Figure 2. (a) XRD and (b)–(d) XPS analyzes for GO and rGO synthesized under hydrothermal condition of 5 h, 180 °C.

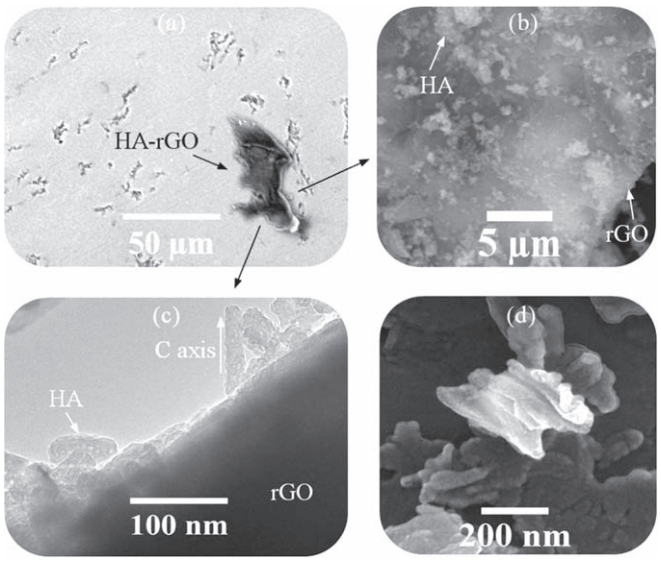

Figure 3. (a) SEM image of consolidated sample, (b) FESEM image of HA-rGO powders, (c) TEM image of HA-rGO powders, (d) FESEM image of HA-rGO after SPS.

Table 1. Specifications for the analytical methods and devices.

Characterization technique	Device	Specification
XRD	X' Pert Pro, Panalytical Co	Cu Kα radiation ($\lambda = 1.54$ Å, 40 kV, 40 mA)
FESEM	Hitachi S4700	equipped with energy dispersive X-ray spectroscopy
Portable SEM	TM-1000	Au coated by sputtering
HRTEM	TALOS F200A	X-FEG electron source, Ceta 16M camera
XPS	Thermo ESCALAB	250XI

2.3. Characterization techniques

Table 1 shows the specifications for the analytical methods and devices [34, 37]. A diamond nail was used to evaluate the nanocomposite's resistance to scratch. Also, ImageJ, CasaXPS, Origin pro 2016, and Diamond 3.2 softwares were used in this study.

3. Results and discussion

Figure 2 shows the XRD and XPS analyzes for GO and rGO synthesized under similar conditions. To investigate the effect of hydrothermal conditions on the reduction of GO, some rGO powders was prepared under the same conditions as HA-rGO. The XRD patterns (figure 2(a)) showed that GO had a peak in the range of $2\theta \approx 10$ deg. As a result of the reduction, this peak disappeared and a new peak appeared in the range of $2\theta \approx 26$ deg. Also, the XPS patterns of GO, rGO, the presence of marked bands (O–C=O, C–O, C=O, and sp^2 C), and the specific displacements in these patterns (figures 2(b)–(d)) showed that GO was well reduced under hydrothermal conditions [19, 38].

Figure 3 shows the SEM image of consolidated sample, FESEM and TEM images of HA-rGO powders and FESEM images of HA-rGO nanocomposite after SPS. In figure 3(a), the large black spot corresponded to the rGO sheets that their surfaces were covered with HA nanorods. Figures 3(b) and (c) are the images of the initial powders, as can be seen the rGO sheets were coated with HA particles. HA has positive charge in some crystalline planes due to the presence of calcium sites. Therefore, a strong electrostatic interaction between HA and GO sheets was formed. In addition, a hydrogen interaction between hydroxyl groups from HA and functional groups containing oxygen from rGO planes such as carboxyl, hydroxyl, carbonyl, and epoxy groups occurs, and a good adhesion between HA and graphene may arise. GO basal planes were more covered with epoxy and hydroxyl groups, while carboxyl groups were located at the edges. The charge of the GO surface was negative in terms of functional groups. The structure of GO affected the formation of HA and induced epitaxial and directional growth. Also, as anchoring sites, oxygen-containing groups induced the formation and bonding of particles to the surface of GO. In the chemical precipitation stage, when adding calcium nitrate to a solution

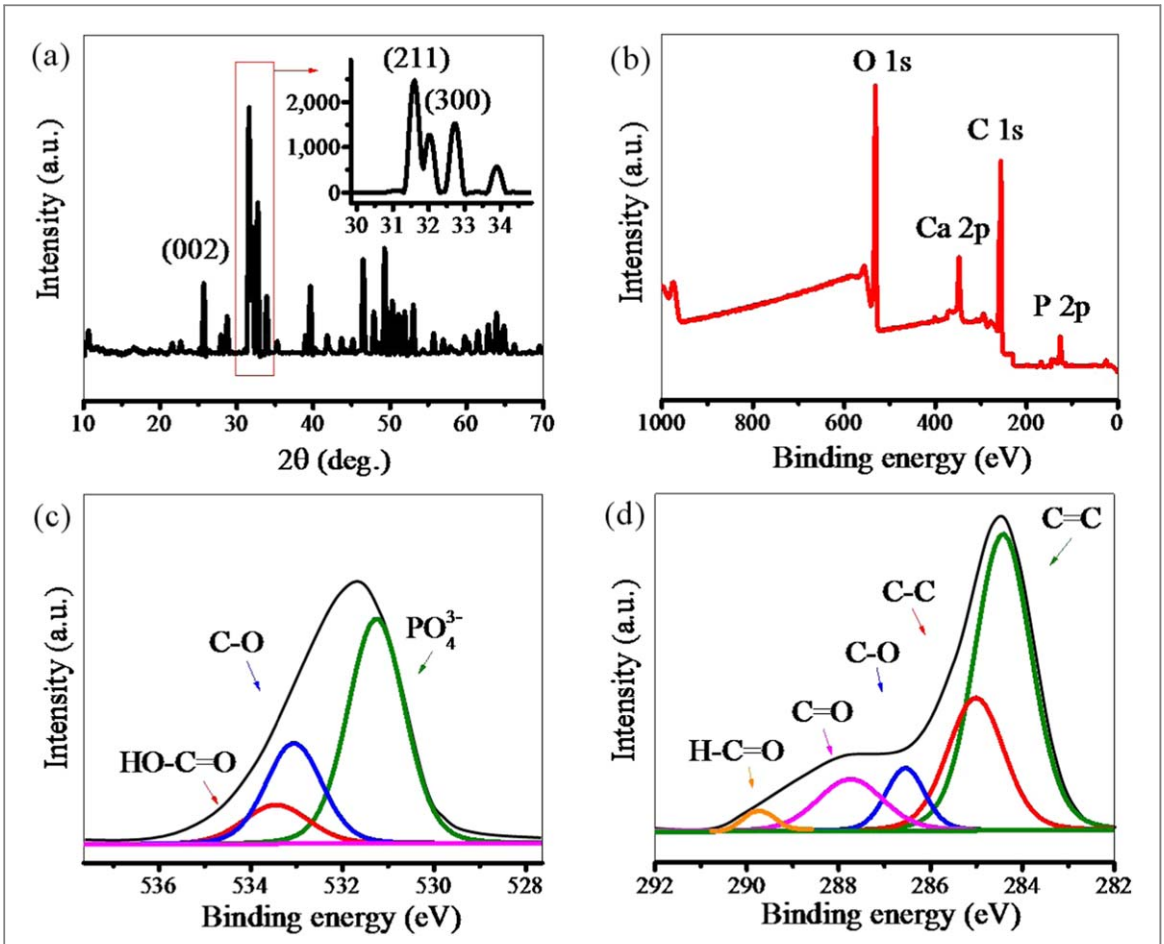

Figure 4. (a) XRD analysis of the HA-rGO nanocomposite, (b) XPS analysis of the HA-rGO nanocomposite, (c), (d) C 1s and O 1s high resolution fitted spectra for the HA-rGO nanocomposite.

containing GO, Ca^{2+} cations were absorbed and bounded to GO by electrostatic interactions with hydroxyl groups or ion exchange with carboxyl groups and played the role of the primary sites for nucleation and growth of HA particles. Calcium ions can react *in situ* with phosphate ions and form calcium phosphate nanoparticles through electrovalence reactions. In this process, the solution was strongly stirred and the rGO layers were homogeneously dispersed, then the same nucleation and the controlled growth occurred. The particles collided several times before connecting to the rGO sheets, which is why a compact structure was formed that had a rod-shaped morphology. The frequency of the collision with the diffusion rate of the growth units, and the reaction rate was determined by the thermodynamic conditions, which depended on the heat transfer rate of the accumulated particles. Most research suggested that HA precipitation occurs more at negative charged sites than positive charged sites, and among the negatively charged groups, phosphate groups have the strongest nucleating for HA [17, 18]. These findings indicated that the HA in this nanocomposite was reinforced with rGO sheets coated with HA. Figure 3(d) also show that the HA nanorods were well sintered. Due to the pressure applied at high temperatures, the morphology of the powders had changed slightly. Due to the coating of rGO sheets with HA and the proper bonding of the HA particles in the sintering process, it was expected that the two-phase bonding (interface) was performed well [34, 39].

Figure 4 shows the XRD and XPS analyzes of the HA-rGO nanocomposite. The XRD pattern of this nanocomposite was consistent with that of pure HA (JCPDS 09-0432) (figure 4(a)). Accordingly, there was no phase other than HA in this nanocomposite, in other words, the HA present in this nanocomposite had not been decomposed at sintering temperature. rGO peaks in this pattern were covered by HA peaks and if it had been oxidized during the sintering operation, it should have seen a long peak at $2\theta \approx 10$ deg. According to these patterns, the $2\theta \approx 26$, 32, 32.3, 33, 35.6, 39.9, and 49.6 correspond to the (002), (211), (112), (300), (202), (310), and (213) crystalline planes, with the d-spacing of 0.343, 0.281, 0.277, 0.271, 0.252, 0.225, and 0.184 nm, respectively. According to the studies, (211), (300), and (002) planes were the main growth planes of HA crystals. And in the case of HA nanorods synthesized by the hydrothermal method, the (002) planes were preferable to the others (*c* axis) [40–44]. According to the XPS pattern (figure 4(b)), P 2p and Ca 2p signals confirmed the presence of HA phase after consolidating process (SPS, 950 °C). In other words, HA phase had retained its

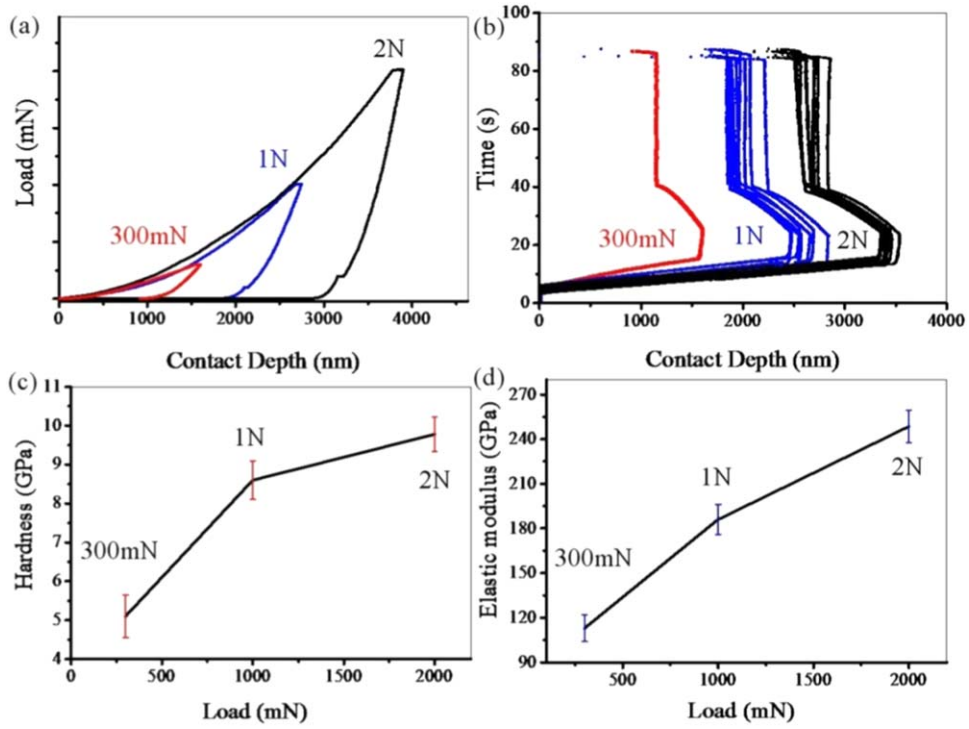

Figure 5. (a) Load-displacement, (b) time-displacement, (c) load-hardness, and (d) load-elastic modulus diagrams.

composition after high temperature sintering and had not been decomposed. According to figures 4(c) and (d), the carboxyl groups of rGO surface still remained the same as the GO, due to the strong electrostatic interaction between carboxyl groups located on the surface of rGO and calcium phosphate [34].

Figure 5 shows the load-displacement, time-displacement, load-hardness, and load-elastic modulus diagrams. Figure 5(a) shows that as the loading rate increased; the slope of the curves in the elastic region was increased, indicating that the elastic modulus was increased. Also, the contact depth at higher loading rates was increased according to figure 5(b). These graphs show that plastic deformation was higher at higher loading rates. As a result, the hardness had increased. According to figures 5(c), (d) (in both graphs) as the loading rate increased from 300 mN to 1 N, the hardness increased with more slope than when the loading rate changes from 1 N to 2 N. As the number of created cracks and their length increased at higher loading rates, the slope of these diagrams decreased at higher loads. In other words, at low loading rates, the energy was spent on plastic and elastic deformation. But at high loading rates, the energy was spent on elastic deformation, plastic deformation, nucleation and growth of created cracks. The hardness and elastic modulus of this composite (hydrothermal process in 5 h) at 1 N loading was equal to the properties of pure HA under similar conditions and the hydrothermal process in 10 h [37]. This indicated that the presence of rGO sheets had a great influence on the mechanical properties because of the lower crystallinity of the powders at low synthesis times. But the effect of rGO was more important in increasing fracture toughness [17, 45].

Figures 6 and 7, and schematic 1 show the HRTEM images of the HA-rGO nanocomposite, the FFT and IFFT analysis along with the schematic images of rGO sheet, rGO cross section, and HA nanorod crystal planes. In the previous studies, the interface between two phases was investigated and it was found that the interface was coherent. Figure 6 provides further details of the HRTEM images. In these analyzes, the honeycomb structure of the rGO sheet is well characterized (figures 6(b), (e)). As is evident, these rGO sheets were well positioned between the HA particles and there was a good connection between the two phases [34]. By comparing the d-spacing of the planes and the properties shown on the schematic images with the atomic images in figures 6 and 7, and schematic 1 a clearer understanding is obtained from the interface between the two phases described before. This kind of coherent interface between the two phases had increased the fracture toughness of HA-rGO nanocomposite. In other words, when the interface between the two phases is coherent, there is a stronger connection between them and the resulting composite strength increases [19].

It is well known in figure 7 that the rGO sheets and the HA particles were fully integrated (figure 7(a)) [34]. In some places, the rGO sheets were interconnected and form a three-dimensional scaffold structure (figure 7(e)). The angle of the (211) planes was about 27 degrees with the rGO surface (figure 7(c)). On the other hand, the

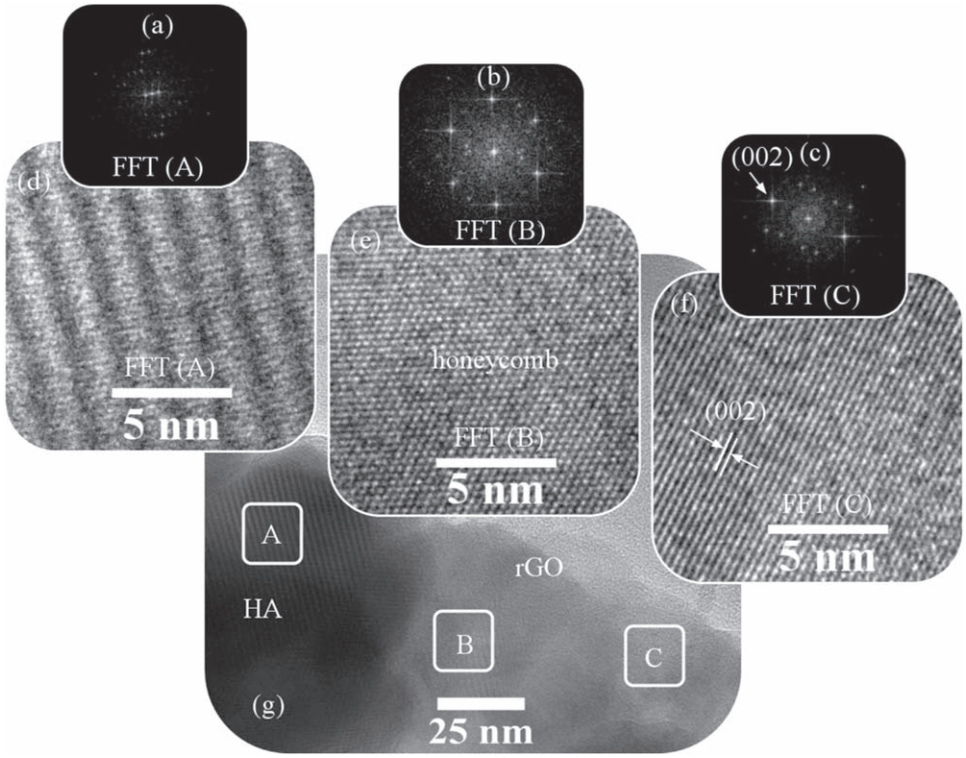

Figure 6. HRTEM images of the HA-rGO nanocomposite along with the FFT and IFFT analysis.

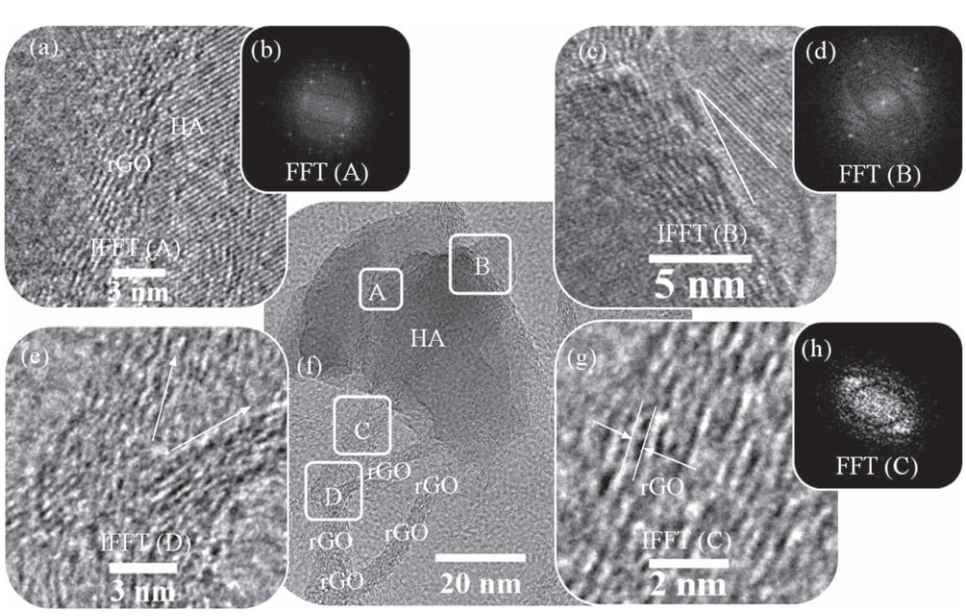

Figure 7. HRTEM images of the HA-rGO nanocomposite along with FFT and IFFT analysis of A, B, C and D areas.

angle between (211) and (300) planes in HA was about 27 degrees. Therefore, the rGO surface was tangible to the HA (300) planes [46, 47]. By comparing FFT analyzes (figure 7(h)), it is found that rGO cross section analysis was galactic.

Figure 8 shows the FESEM images of cracks, the mechanisms for increasing fracture toughness, and the FESEM images of scratch evaluation. Due to the inherent brittleness of HA, cracks in it grow rapidly and lead to failure. The presence of rGO sheets in HA-rGO nanocomposites prevented the growth of these cracks and increased the fracture toughness. The most common mechanisms that increased fracture toughness were rGO sheets bridging, rGO pull-out, crack branching, and crack deflection [17]. In other words, rGO sheets need more energy to be removed due to their high specific surface area. This increased in energy to be removed from the HA

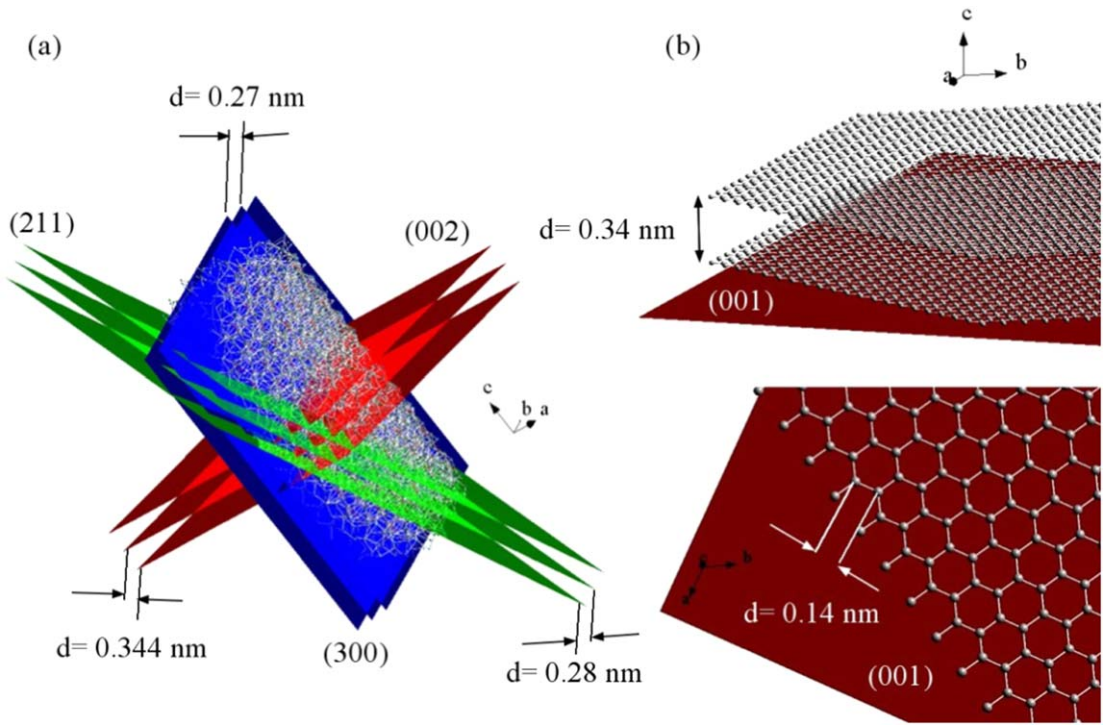

Schematic 1. The schematic images of graphene sheet, rGO cross section, and HA nanorod crystal planes

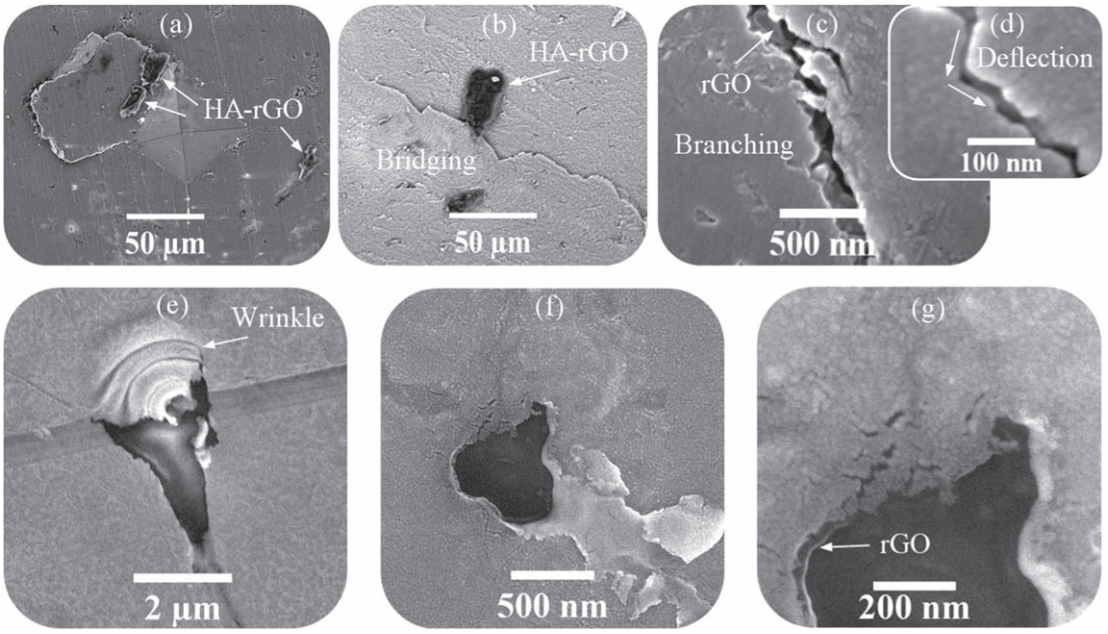

Figure 8. FESEM images of cracks, the mechanisms for increasing fracture toughness, and the FESEM images of scratch evaluation.

phase increased the fracture toughness of HA-rGO nanocomposites [19]. Some of these mechanisms are illustrated in figure 8. In figure 8(a), the Vickers affected zone is known. This section was related to high loads $>$ 2 N. In high loads such destruction occurred but they were much smaller than pure HA, due to the increased nanocomposite fracture toughness. The scratch test results (figures 8(e)–(g)) showed that the presence of rGO sheets had partially controlled the HA brittleness. Folding and wrinkling of rGO sheets had improved the weakness of HA brittleness. The mechanism that improved the brittleness involved the transfer of force that caused the HA particles to disintegrate into rGO sheets. Due to the high specific surface area of rGO sheets, this

force was compensated by rGO folding or transferring force to other particles, and the brittleness was somewhat improved.

4. Conclusions

The findings of this study showed that the HA in this nanocomposite was reinforced with rGO sheets coated with HA. As the loading rate increased, the slope of the curves in the elastic region was increased, indicating that the elastic modulus was increased. Also, the contact depth at higher loading rates was increased. Plastic deformation was higher at higher loading rates and the hardness had increased. As the loading rate increased from 300 mN to 1 N, the hardness and elastic modulus increased with more slope than when the loading rate changed from 1 N to 2 N. The presence of rGO sheets had partially controlled the HA brittleness. The findings of this study could be useful for applications of this nanocomposite.

Data availability

Schematic images of crystals were drawn with Diamond (3.2) software and it can be found through the link: https://www.crystalimpact.com/diamond/. Other schematic images, diagrams, and images were prepared by employing the Powerpoint (2007), Originpro (2016), CasaXPS, and ImageJ (1.52P) softwares that can be found through the links: https://products.office.com/en-us/home, https://www.originlab.com/origin, http://www.casaxps.com/, and https://imagej.nih.gov/ij/download.html, respectively. Other data will be made available on request.

ORCID iDs

Hassan Nosrati https://orcid.org/0000-0003-1509-9819
Rasoul Sarraf-Mamoory https://orcid.org/0000-0001-8688-8853

References

[1] Fadol H, Yafei SGA, Uzun K, Musharavati F, Zalnezhad E, Hamouda AMS, Yun CO and Jaber F 2018 HA/rGO/Pd nanocomposite thin film coating on SST 304—synthesize, characterization, and properties investigations *J. Alloys Compd.* **741** 562–74
[2] Đošic M, Erakovic S, Jankovic A, Vukašinovic-Sekulic M, Matic IZ, Stojanovic J, Rhee KY, Miškovic-Stankovic V and Park SJ 2017 *In vitro* investigation of electrophoretically deposited bioactive hydroxyapatite/chitosan coatings reinforced by graphene *J. Ind. Eng. Chem.* **47** 336–47
[3] Chen X, Zhang B, Gong Y, Zhou P and Li H 2018 Mechanical properties of nanodiamond-reinforced hydroxyapatite composite coatings deposited by suspension plasma spraying *Appl. Surf. Sci.* **439** 60–5
[4] Türk S, Altınsoy I, Efe GG, Ipek M, Ozacar M and Bindal C 2018 The effect of reduction of graphene oxide on the formation of hydroxyapatite and tricalcium phosphate *Vacuum* **148** 1–10
[5] Nie W, Peng C, Zhou X, Chen L, Wang W, Zhang Y, Ma PX and He C 2017 Three-dimensional porous scaffold by self-assembly of reduced graphene oxide and nano-hydroxyapatite composites for bone tissue engineering *Carbon* **116** 325–37
[6] Moldovan M, Prodan D, Sarosi C, Carpa R, Socaci C, Rosu MC and Pruneanu S 2018 Synthesis, morpho-structural properties and antibacterial effect of silicate based composites containing graphene oxide/hydroxyapatite *Mater. Chem. Phys.* **217** 48–53
[7] Kaneko N *et al* 2020 Development of nitrogen-doped hydroxyapatite ceramics *Journal of Asian Ceramic Societies* **8** 130–7
[8] Lee JJ, Shin YC, Song SJ, Cha JM, Hong SW, Lim YJ, Jeong SJ, Han DW and Kim B 2018 Dicalcium phosphate coated with graphene synergistically increases osteogenic differentiation *In Vitro Coatings* **8** 1–12
[9] Fu C, Bai H, Zhu J, Niu Z, Wang Y, Li J, Yang X and Bai Y 2017 Enhanced cell proliferation and osteogenic differentiation in electrospun PLGA/hydroxyapatite nanofibre scaffolds incorporated with graphene oxide *PLoS One* **12** 1–20
[10] Mehrali M, Moghaddam E, Shirazi SFS, Baradaran S, Mehrali M, Latibari ST, Metselaar HSC, Kadri NA, Zandi K and Osman NAA 2014 Synthesis, mechanical properties, and *in vitro* biocompatibility with osteoblasts of calcium silicate−reduced graphene oxide composites *ACS Appl. Mater. Interfaces* **6** 3947–62
[11] Gholibegloo E, Karbasi A, Pourhajibagher M, Chiniforush N, Ramazani A, Akbari T, Bahador A and Khoobi M 2018 Carnosine-graphene oxide conjugates decorated with hydroxyapatite as promising nanocarrier for ICG loading with enhanced antibacterial effects in photodynamic therapy against *Streptococcus mutans Journal of Photochemistry & Photobiology, B: Biology* **181** 14–22
[12] Gao C, Feng P, Peng S and Shuai C 2017 Carbon nanotube, graphene and boron nitride nanotube reinforced bioactive ceramics for bone repair *Acta Biomater.* **61** 1–20
[13] Nosrati H, Sarraf-Mamoory R, Ahmadi AH and Perez MC 2020 Synthesis of graphene nanoribbons–hydroxyapatite nanocomposite applicable in biomedicine and theranostics *J. Nanotheranostics* **1** 1–13
[14] Mišković-Stanković V, Eraković S, Janković A, Vukašinović-Sekulić M, Mitrić M, Jung YC, Park SJ and Rhee KY 2015 Electrochemical synthesis of nanosized hydroxyapatite/graphene composite powder *Carbon Letters* **16** 233–40
[15] Nosrati H, Sarraf-Mamoory R and Dabir F 2019 Crystallographic study of hydrothermal synthesis of hydroxyapatite nano-rods using Brushite precursors *Journal of Tissues and Materials* **2** 1–8
[16] Ramadas M, Bharath G, Ponpandian N and Ballamurugan AM 2017 Investigation on biophysical properties of hydroxyapatite/graphene oxide (HAp/GO) based binary nanocomposite for biomedical applications *Mater. Chem. Phys.* **199** 179–84

[17] Baradaran S, Moghaddam E, Basirun WJ, Mehrali M, Sookhakian M, Hamdi M, Moghaddam MRN and Alias Y 2014 Mechanical properties and biomedical applications of a nanotube hydroxyapatite-reduced graphene oxide composite *Carbon* **69** 32–45
[18] Nosrati H, Sarraf Mamoory R, Dabir F, Le DQS, Bünger CE, Perez MC and Rodriguez MA 2019 Effects of hydrothermal pressure on *in situ* synthesis of 3D graphene/hydroxyapatite nano structured powders *Ceram. Int.* **45** 1761–9
[19] Nosrati H, Sarraf-Mamoory R, Le DQS and Bünger CE 2020 Enhanced fracture toughness of three dimensional graphene-hydroxyapatite nanocomposites by employing the Taguchi method *Composites Part* B **190** 107928
[20] Liu Y, Huang J, Niinomi M and Li H 2016 Inhibited grain growth in hydroxyapatite–graphene nanocomposites during high temperature treatment and their enhanced mechanical properties *Ceram. Int.* **42** 11248–55
[21] Zhang L, Liu W, Yue C, Zhang T, Li P, Xing Z and Chen Y 2013 A tough graphene nanosheet/hydroxyapatite composite with improved *in vitro* biocompatibility *Carbon* **61** 105–15
[22] Wang S, Zhang S, Wang Y, Sun X and Sun K 2017 Reduced graphene oxide/carbon nanotubes reinforced calcium phosphate cement *Ceram. Int.* **43** 13083–8
[23] Elif Ö, Belma Ö and İlkay Ş 2017 Production of biologically safe and mechanically improved reduced graphene oxide/hydroxyapatite composites *Mater. Res. Express* **4** 1–12
[24] Liu Y, Huang J and Li H 2013 Synthesis of hydroxyapatite–reduced graphite oxide nanocomposites for biomedical applications: oriented nucleation and epitaxial growth of hydroxyapatite *J. Mater. Chem.* B **1** 1826–34
[25] Zhao Y, Sun KN, Wang WL, Wang YX, Sun XL, Liang YJ, Sun XN and Chui PF 2013 Microstructure and anisotropic mechanical properties of graphene nanoplatelet toughened biphasic calcium phosphate composite *Ceram. Int.* **39** 7627–34
[26] Xiao H, Wang X, Long C, Liu Y, Yin A and Zhang Y 2018 Investigation of the mechanical properties of ZrO_2-doped UO_2 ceramic pellets by indentation technique *J. Nucl. Mater.* **509** 482–7
[27] Silva AP, Booth F, Garrido L, Aglietti E, Pena P and Baudín C 2018 Young's modulus and hardness of multiphase $CaZrO_3$-MgO ceramics by micro and nanoindentation *J. Eur. Ceram. Soc.* **38** 2194–201
[28] Labonte D, Lenz AK and Oyen ML 2017 On the relationship between indentation hardness and modulus, and the damage resistance of biological materials *Acta Biomater.* **57** 373–83
[29] Tiegel M, Hosseinabadi R, Kuhn S, Herrmann A and Rüssel C 2015 Young's modulus, Vickers hardness and indentation fracture toughness of alumino silicate glasses *Ceram. Int.* **41** 7267–75
[30] Maiti P, Bhattacharya M, Das PS, Devi PS and Mukhopadhyay AK 2018 Indentation size effect and energy balance issues in nanomechanical behavior of ZTA ceramics *Ceram. Int.* **44** 9753–72
[31] Nastic A, Merati A, Bielawski M, Bolduc M, Fakolujo O and Nganbe M 2015 Instrumented and Vickers indentation for the characterization of stiffness, hardness and toughness of zirconia toughened Al_2O_3 and SiC armor *Journal of Materials Science & Technology* **31** 773–83
[32] Sohn Y, Bae M, Song I, Chu K, Kim D and Han I 2012 Embrittlement study of electroplated nickel films by microindentation *Scr. Mater.* **67** 919–22
[33] Jin Y, Zhang T, Lui YF, Sze KY and Lu WW 2020 The measured mechanical properties of osteoporotic trabecular bone decline with the increment of deformation volume during micro-indentation *J. Mech. Behav. Biomed. Mater.* **103** 103546
[34] Nosrati H, Sarraf-Mamoory R, Le DQS and Bünger CE 2019 Preparation of reduced graphene oxide/hydroxyapatite nanocomposite and evaluation of graphene sheets/hydroxyapatite interface *Diamond & Related Materials* **100** 107561
[35] Ahmadi AH, Nosrati H and Sarraf-Mamoory R 2019 Decreasing β-three calcium phosphate particle size using graphite as nucleation sites and diethylene glycol as a chemical additive *Journal of Bioengineering Research* **1** 50–8
[36] Oliver W and Pharr G 1992 An improved technique for determining hardness and elastic modulus using load and displacement sensing indentation experiments *J. Mater. Res.* **7** 1564–83
[37] Nosrati H, Sarraf Mamoory R, Le DQS, Bünger CE, Emameh RZ and Dabir F 2020 Gas injection approach for synthesis of hydroxyapatite nanorods via hydrothermal method *Mater. Charact.* **159** 110071
[38] Johra FT and Jung WG 2015 Hydrothermally reduced graphene oxide as a supercapacitor *Appl. Surf. Sci.* **357** 1911–4
[39] Shin YC, Lee JH, Jin OS, Kang SH, Hong SW, Kim B, Park JC and Han DW 2015 Synergistic effects of reduced graphene oxide and hydroxyapatite on osteogenic differentiation of MC3T3-E1 preosteoblasts *Carbon* **95** 1051–60
[40] Lee JH, Shin YC, Lee SM, Jin OS, Kang SH, Hong SW, Jeong CM, Huh JB and Han DW 2015 Enhanced osteogenesis by reduced graphene oxide/hydroxyapatite nanocomposites *Sci. Rep.* **5** 1–13
[41] Bharath G, Madhu R, Chen SM, Veeramani V, Balamurugan A, Mangalaraj D, Viswanathan C and Ponpandian N 2015 Enzymatic electrochemical glucose biosensors by mesoporous 1D hydroxyapatite-on-2D reduced graphene oxide *J. Mater. Chem.* B **3** 1360–70
[42] Xie X, Hu K, Fang D, Shang L, Tran SD and Cerruti M 2015 Graphene and hydroxyapatite self-assemble into homogeneous, free standing nanocomposite hydrogels for bone tissue engineering *Nanoscale* **7** 7992–8002
[43] Yao C, Zhu J, Xie A, Shen Y, Li H, Zheng B and Wei Y 2017 Graphene oxide and creatine phosphate disodium dual template-directed synthesis of GO/hydroxyapatite and its application in drug delivery *Materials Science and Engineering* C **73** 709–15
[44] Nosrati H, Sarraf-Mamoory R, Le DQS and Bünger CE 2020 Fabrication of gelatin/hydroxyapatite/3D-graphene scaffolds by a hydrogel 3D-printing method *Mater. Chem. Phys.* **239** 122305
[45] Ding M, Sahebgharani N, Musharavati F, Jaber F, Zalnezhad E and Yoon GH 2018 Synthesis and properties of HA/ZnO/CNT nanocomposite *Ceram. Int.* **44** 7746–53
[46] Zhang Q, Liu Y, Zhang Y, Li H, Tan Y, Luo L, Duan J, Li K and Banks CE 2015 Facile and controllable synthesis of hydroxyapatite/graphene hybrid materials with enhanced sensing performance towards ammonia *Analyst* **140** 5235–42
[47] Nosrati H, Sarraf-Mamoory R, Le DQS, Perez MC and Bünger CE 2020 Evaluation of argon-gas-injected solvothermal synthesis of hydroxyapatite crystals followed by high-frequency induction heat sintering *Cryst. Growth Des.* **20** 3182–9